Journal of Applied Fluid Mechanics, Vol. 18, No. 12, pp. 3082-3100, 2025.
Available online at www.jafmonline.net, ISSN 1735-3572, EISSN 1735-3645.
https://doi.org/10.47176/jafm.18.12.3597

Experimental and Numerical Investigation on Gas–liquid Two-phase Flow Dynamics and Pressure Drop in Horizontal Contraction Pipes

J. Wen[1], Y. Ren[1], D. Wang[2] and C. Bai[1†]

[1] *State Key Laboratory for Strength and Vibration of Mechanical Structures / Shaanxi Key Laboratory of Environment and Control for Flight Vehicle, Xi'an Jiaotong University, Xi'an 710049, China*
[2] *Xi'an Thermal Power Research Institute Co., Ltd., Xi'an, 710054, China*

†*Corresponding Author Email: baichq@mail.xjtu.edu.cn*

ABSTRACT

Contraction pipes are widely employed in pipeline systems to enable transitions between varying pipe diameters. The behavior of two-phase flow within these pipes and the resulting internal pressure drop can significantly influence the operation and safety of such systems. To explore the mechanisms linking two-phase pressure drop characteristics to flow patterns in horizontal contraction pipes, we designed and constructed an experimental setup. The pressure variations within the contraction pipe under different operating conditions were measured experimentally, and the phenomenon of vena contracta for two-phase flow with different flow patterns was analyzed using the Ω-vortex identification method based on the numerical simulation results. Stratified flow in contraction pipes exhibits significant interphase interactions, which inhibit the formation of vena contracta and impact pressure drop characteristics. Intermittent flow displays hybrid behaviors: resembling single-phase flow during liquid slug transit (with transient vena contracta formation) and stratified flow during gas bubble passage (suppressing vena contracta). By examining the vena contracta phenomenon across various flow patterns, we develop an improved pressure drop model for contraction pipes, extending the homogeneous flow model by incorporating a flow-pattern-dependent contraction coefficient. The pressure drop predicted by the improved model agrees with the experimental data within a 20% error band for 95% of the data points, demonstrating the validity of the proposed model. Compared with the homogeneous flow model, the improved model reduces the mean relative error by 12.52% and enhances the prediction accuracy of the contraction pressure drop for two-phase flow.

Article History

Received April 11, 2025
Revised June 12, 2025
Accepted July 18, 2025
Available online October 6, 2025

Keywords:

Gas-liquid two-phase flow
Contraction
Pressure drop
Flow pattern
Vena contracta

1. INTRODUCTION

Pipeline transportation offers several advantages, including structural simplicity, high efficiency, and energy conservation. Consequently, it is extensively utilized in the petrochemical, nuclear energy, and aerospace industries. Over the past few decades, extensive research has been conducted on single-phase flow pipelines conveying gas or liquid media, primarily focusing on the internal pressure drop and flow characteristics. However, gas–liquid two-phase flows exhibit significantly more complex flow behaviors and have attracted considerable research interest because of their critical roles in diverse industrial applications. Therefore, investigating the pressure drop and flow characteristics of a two-phase flow in these systems is crucial to enhancing operational safety, optimizing energy efficiency, and improving overall system performance.

Since the 1940s, extensive research has been devoted to characterizing the pressure drop and flow behavior of two-phase flows in pipelines, resulting in the development of numerous predictive models for two-phase pressure drops. Researchers have primarily classified frictional losses in straight pipes into two categories based on fundamental assumptions: homogeneous and separated flow models. The former approach conceptualizes a two-phase flow as a pseudo-fluid with homogenized properties derived from the weighted averages of the liquid and gas phases (Beattie & Whalley, 1982; Lin et al., 1991; McAdams et al., 1942; Shannak, 2008). The latter postulates an artificial separation of phases, assuming constant phase velocities within their respective occupied

NOMENCLATURE

A_2	cross-sectional area of outlet pipe	V_L	volumetric flow rate of liquid
A_c	minimum cross-sectional area at vena contracta	v_G	volume occupied by the gas phases within an intermittent unit
C	empirical coefficient	v_L	volume occupied by the liquid phases within an intermittent unit
C_c	contraction coefficient	X	Martinelli parameter
D_1	inner diameter of the inlet pipe	x	flow quality
D_2	inner diameter of the outlet pipe	Δp_c	contraction pressure drop
f_s	liquid slug fraction in intermittent flow	Δp_{in}	frictional pressure losses from upstream measurement point to contraction segment
G_2	mass flow rate at the outlet pipe	Δp_{LO}	the pressure drop when the liquid phase flows through an identical pipe alone
h	liquid film height under gas bubbles	Δp_{out}	frictional pressure losses from downstream measurement point to contraction segment
h_f	pressure loss	Δp_{tot}	total measured pressure drop
K_c	pressure loss coefficient	Δp_{TP}	pressure drop experienced in the two-phase flow through the pipe
L	axial length of the contraction segment	α	void fraction
L_1	axial distance from the upstream pressure sensor to the contraction inlet	α_f	ratio between liquid film cross-sectional area in liquid film region and pipe cross-sectional area.
L_2	axial distance from the downstream pressure sensor to the contraction outlet	β	volumetric gas fraction
L_f	length of the liquid film region in intermittent flow	θ	opening angle of the contraction segment
L_s	length of the liquid slug region in intermittent flow	Φ_{LO}^2	liquid-only two-phase multiplier
S	slip ratio	ρ_G	gas density
U_{gs}	gas superficial velocity	ρ_L	liquid density
U_{ls}	liquid superficial velocity	ρ_m	mean density of the two-phase flow
U_m	mean velocity of two-phase flow	σ_A	area ratio
V	volumetric flow rate	σ_D	diameter ratio
V_G	volumetric flow rate of gas	Ω	vortex identification parameter

zones (Cavallini et al., 2002; Chen et al., 2001; Chisholm, 1967; Friedel, 1979; Mishima & Hibiki, 1996). Notably, emerging evidence from recent decades reveals a critical connection between frictional pressure losses and two-phase flow patterns (Cheng et al., 2008b; Moreno Quiben, 2005; Quibén & Thome, 2007a, 2007b). This correlation underscores the importance of flow pattern analysis, as these interfacial configurations, which are governed by the phase superficial velocities, fluid properties, and system operating conditions (Monni et al., 2014), fundamentally dictate the momentum and energy transfer mechanisms of the two-phase flow. Consequently, focusing on specific flow patterns enhances the prediction accuracy of two-phase frictional losses along pipelines. In a study on two-phase flow patterns, Vallée et al. (2008) experimentally and numerically analyzed horizontal stratified air–water flows, focusing on slug flow initiation and computational fluid dynamics (CFD) validation for interfacial instability-driven regime transitions. Ong and Thome (2011) identified confinement thresholds governing two-phase flow pattern transitions in small channels, highlighting the suppressed stratification under surface tension dominance. Akhlaghi et al. (2019) numerically simulated intermittent flow in a horizontal pipe using a multi-fluid volume-of-fluid (VOF) model, and the simulation results accurately matched the experimental results. Amini et al. (2023) analyzed the flow pattern transition in a liquid–liquid two-phase flow within a serpentine microchannel. The influence of flow patterns extends beyond frictional losses to encompass localized pressure losses caused by pipeline components. Industrial pipeline systems inherently have geometric discontinuities such as reducers, elbows, valves, tees, and orifices. These components induce abrupt flow-boundary alterations, generating secondary flows, flow separation, and turbulent vortices. Collectively, these factors contribute to localized energy dissipation. Significant research efforts have been directed toward understanding the two-phase pressure drop and flow characteristics of these components. El-Shaboury et al. (2007) experimentally studied an air–water two-phase flow in a horizontal impacting tee junction, generating phase distribution and pressure drop data for wavy, stratified, and annular inlet flow patterns. Zhang et al. (2021) investigated the transient characteristics of a stratified flow through an orifice plate using the VOF method. They found that the liquid volume ratio significantly affects the behavior of two-phase jet flows. Zahedi and Rad (2022) investigated gas–liquid slug flow in 90° elbows via experiments and CFD, showing that the curvature radius modulates the turbulence intensity and frequency bandwidth while maintaining slug flow stability. A notable contribution was made by Zeghloul et al. (2017, 2018, 2020), who systematically investigated two-phase flow through orifices, multi-hole orifices, ball valves, and gate valves across various flow patterns. Their work demonstrated that different flow patterns result in distinct

pressure drop variation trends, confirming the universal importance of flow patterns in both frictional and localized losses. This understanding is beneficial for analyzing components that feature abrupt geometric transitions, such as contraction pipes.

In engineering pipeline systems, contraction pipes are essential transitional components that ensure the hydraulic continuity between pipes of different diameters. These structures are geometrically classified into two primary types: gradual and sudden structures. To assess the two-phase hydraulic behavior of such geometries, Kourakos et al. (2009) conducted experimental investigations of pressure drop characteristics across contraction pipes, whereas Ahmadpour et al. (2016) performed numerical simulations focusing on the two-phase pressure distribution in contractions with various opening angles. Both studies consistently revealed that pressure loss increased with larger opening angles and smaller area ratios of contraction. Although these studies established fundamental relationships between the geometric parameters and pressure losses, the complex interactions and specific flow phenomena of two-phase flows require further investigation. Abdelall et al. (2005) conducted an experimental study on the pressure drop induced by an abrupt flow area contraction in small circular channels and proposed a novel pressure drop correlation derived from the assumption of minimum entropy production. Padilla et al. (2013) quantified the perturbation lengths upstream and downstream of contraction pipes and established a two-phase pressure drop model by incorporating frictional loss within these perturbation regions. In single-phase flows through contractions, flow separation from the pipe wall generates vena contracta, which is a critical phenomenon that fundamentally alters the velocity profile and dictates pressure recovery characteristics. However, the extension of this concept to multiphase systems remains controversial. Al'Fer-ov and Shul'Zhenko (1977) and Attou and Bolle (1995) posited that the vena contracta phenomenon occurs in a manner analogous to single-phase flow. They also examined the dispersed droplet flow pattern that emerges downstream of the vena contracta point. Schmidt and Friedel (1997) experimentally demonstrated the absence of an axial pressure minimum in two-phase contraction, thus refuting the existence of vena contracta. However, their investigation did not analyze flow pattern dependencies. In contrast, Chen et al. (2008a) revealed flow-pattern-dependent vena contracta behavior through an experimental investigation of sudden contractions in small rectangular channels. Their data exhibited a distinct local peak in the pressure drop magnitude versus flow quality curves corresponding to the transition from annular to slug flow. This led them to postulate that distinct flow patterns exhibit differential vena contracta phenomena, which affect the magnitude of the pressure drop. To complement these experimental limitations, subsequent numerical investigations employing 2D axisymmetric Eulerian–Eulerian models (Roul & Dash, 2011; Patra et al., 2021) have extended the experimental work of Schmidt and Abdelall. These simulations revealed distinct vena contracta and flow characteristics between two- and single-phase systems. Nevertheless, the inherent limitations of these numerical methods prevent them from capturing differences in flow patterns. Existing research has demonstrated that the two-phase pressure drop is correlated with flow patterns. However, studies focusing on pressure drop variations across different flow patterns remain limited, and the mechanisms underlying the influence of flow patterns on the pressure drop have not been fully elucidated. Therefore, predicting the pressure drop based on flow patterns has become a critical focus of current research on two-phase flows. For contraction pipes, further investigation is required to elucidate the mechanisms underlying the interaction between flow patterns and pressure drop, particularly with respect to the vena contracta phenomenon.

This study experimentally investigated the pressure drop characteristics of single-phase, stratified, and intermittent flows in a contraction pipe under varying flow conditions. Focusing on the vena contracta phenomenon, we employed numerical simulations to explore the flow characteristics and mechanisms influencing the pressure drop in single- and two-phase flows. A method for determining the contraction coefficient of a two-phase flow with various flow patterns was developed based on a comprehensive analysis of the flow characteristics of diverse flow patterns. Subsequently, an improved two-phase pressure-drop model was developed for contraction pipes, which extends the homogeneous flow model by considering the flow-pattern effect. The accuracy of the proposed model was supported by experimental verification, which demonstrated its high precision.

2. Two-Phase Flow Experimental Setup and Numerical Simulation Model

An experimental setup was designed and constructed to investigate the pressure drop and flow characteristics of a gas–liquid two-phase flow with different patterns in a contraction pipe. Controlled gas and liquid flow-rate variations were applied to examine the pressure-drop characteristics across different flow patterns. Parallel to the experimental work, a corresponding CFD simulation model was developed in ANSYS FLUENT using the actual geometric dimensions of the contraction pipe from the experimental setup.

2.1 Experimental Setup and Operating Conditions

The experimental setup consisted of a gas–liquid recirculating system using air and water as the working fluids. As depicted in Fig. 1, the system comprised three core modules: a gas–liquid supply unit, experimental loop, and measurement unit. The gas and liquid, pressurized by an air compressor (BMVF7.5) and a horizontal centrifugal pump (ZS50-32-200/4.0), respectively, flowed through independent branches equipped with flowmeters to ensure predetermined flow rates. These phases were mixed in a gas–liquid mixer before entering the experimental loop. The main horizontal channel consisted of three primary sections: the flow development section, with a length 66 times the inner diameter of the outlet pipe; the contraction pipe, specifically designed for testing purposes; and the outlet pipe connected to the pressure vessel used to maintain a stable back pressure. The gas–liquid separator

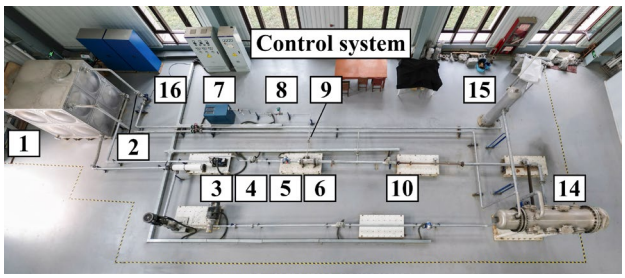

(a) Two-phase flow experimental setup

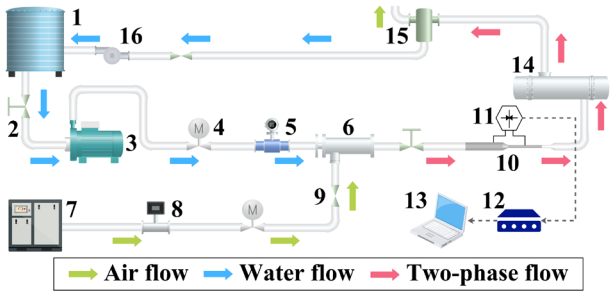

(b) Schematic diagram of the experimental flow path

l-Water tank; 2-Manual valve; 3-Horizontal centrifugal pump; 4-Electric valve; 5-Electromagnetic flowmeter; 6-Gas–liquid mixer; 7-Air compressor; 8-Vortex flowmeter; 9-Check valve; 10-Test section; 11-Pressure sensors; 12-DAQ System; 13-Computer; 14-Pressure vessel; 15-Gas–liquid separator; 16-Centrifugal pump.

Fig. 1 Two-phase flow experimental setup and flow path diagram

ensured phase segregation, with the gas vented into the atmosphere, whereas the liquid returned to the water tank via a centrifugal pump on the recirculation line, thereby achieving closed-loop operation.

In the two-phase flow experiments, distinct flow patterns were established by controlling the variations in gas and liquid flow rates. Gas flow regulation was achieved by precisely adjusting the control valve in the branch, whereas the liquid flow was regulated using a variable-frequency drive on the horizontal centrifugal pump. For the gas flow measurements, two vortex flowmeters with overlapping ranges (0–12 m^3/h and 6–35 m^3/h) were employed, each with a measurement uncertainty of ±1% to ensure precision. The liquid flow was quantified using an electromagnetic flowmeter with a range of 0–200 m^3/h and uncertainty of ±0.5%. As shown in Fig. 2, the two-phase pressure drop was measured using a dedicated pressure monitoring system featuring an array of calibrated PCB Model 1501 pressure sensors (±0.25% sensitivity). These sensors were mounted at L_1=2D_1 upstream and L_2=8D_2 downstream of the contraction pipe, where D_1 and D_2 denote the inner diameters of the inlet and outlet pipes, respectively. The sensors were operated within the 0–1 MPa absolute-pressure range. Signal acquisition was performed using a CoCo-80X Dynamic Signal Analyzer (DSA; Crystal Instruments), which provides a 150 dBFS dynamic range and configurable sampling frequencies from 0.48 Hz to 102.4 kHz. During the experiments, the DSA sampled pressure signals at 12

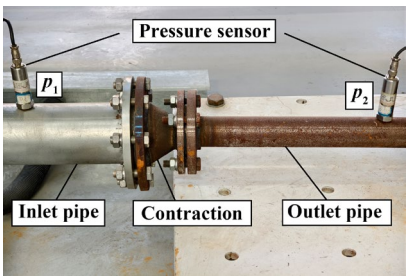

(a) Test section and pressure sensors

(b) Data acquisition instrument and DC power supply

Fig. 2 Test section and measurement unit

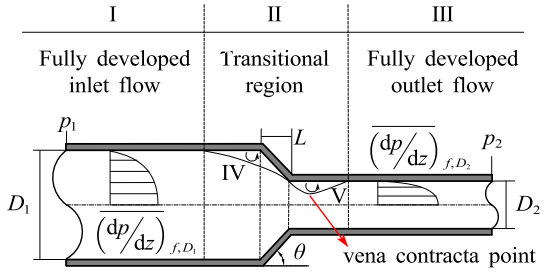

(a) Test section schematic and internal flow

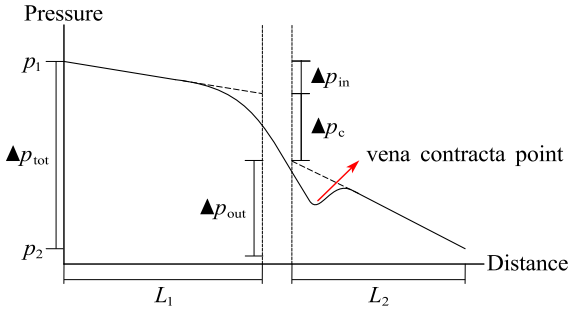

(b) Idealized pressure distribution in the test section

Fig. 3 Test section configuration and idealized flow field

kHz. To ensure stable data acquisition, we calculated the localized pressure values as the arithmetic mean of five replicate measurements per operational condition. Each measurement lasted for 2 min to minimize random errors inherent to the system.

The contraction pressure drop uncertainties were evaluated by propagating errors from flowmeters (±1% for gas, ±0.5% for liquid) and pressure sensors (±0.25%). We considered V_L=20 m^3/h and V_G=30 m^3/h as examples. The total expanded uncertainty (95% confidence) was ±2.06%, ensuring the reliability of experimental results.

Figure 3 shows a schematic of the test section used in the experimental setup, with the key geometric dimensions

Table 1 Dimension parameters of the test section

Parameters	Values
D_1 (mm)	100.00
D_2 (mm)	50.00
σ_D (-)	0.50
σ_A (-)	0.25
L (mm)	45.00
θ (°)	29.05

annotated in Fig. 3(a). The diameter ratio is defined as $\sigma_D = D_2/D_1$, and the area ratio is defined as $\sigma_A = \sigma_D^2 = D_2^2/D_1^2$. The contraction length L denotes the axial distance between the inlet and outlet sections, and θ is the opening angle of the contraction. The dimension parameter values adopted in this study are presented in Table 1.

As shown in Fig. 3(a), Region II comprised two subregions: eddy zone IV, which was distinguished by the presence of flow separation and recirculation eddies in proximity to the contraction inlet, and contraction zone V, which was characterized by flow acceleration resulting in a vena contracta. This vena contracta corresponded to a localized jet flow with a minimum cross-sectional area, A_c, which aligned with the position of the local minimum pressure observed in Fig. 3(b). The contraction coefficient is defined as $C_c = A_c/A_2$, where A_2 is the cross-sectional area of the outlet pipe. A contraction coefficient of $C_c = 1$ indicates the absence of vena contracta formation (Chalfi & Ghiaasiaan, 2008).

Figure 3(b) shows the idealized axial pressure distribution profile within the contraction pipe. Regions I and III correspond to the fully developed flow zones, where the axial pressure gradient dp/dz remained constant because of the steady frictional losses along the pipe walls, resulting in a linear pressure drop along the axial direction. Therefore, the total experimentally measured pressure drop Δp_{tot} comprised two components: the frictional pressure loss, governed by the linear pressure gradient in Regions I and III, and the contraction pressure drop Δp_c, resulting from the flow acceleration and turbulence in the contraction segment. To isolate Δp_c, we extrapolated the linear pressure trends from Regions I and III to the contraction boundaries (dashed lines in Fig. 3(b)):

$$\Delta p_c = \Delta p_{tot} - \Delta p_{in} - \Delta p_{out} = \Delta p_{tot} - L_1\left(\frac{dp}{dz}\right)_{f,D_1} - L_2\left(\frac{dp}{dz}\right)_{f,D_2} \quad (1)$$

where Δp_{in} and Δp_{out} denote the frictional pressure losses from the upstream and downstream measurement points to the contraction segment, respectively. The gradient dp/dz was obtained from independent friction measurements in a straight pipe of identical diameter and roughness as the upstream and downstream pipes, with a length of 2 m (ensuring fully developed flow), under matching flow conditions.

For the pressure drop measurements, a comprehensive experiment comprising 96 tests was conducted. This included 88 gas–liquid two-phase flow tests with gas superficial velocities U_{gs} ranging from 0.071 to 1.203 m/s and liquid superficial velocities U_{ls} from 0.071 to 0.884 m/s, along with eight single-phase liquid flow tests conducted at identical liquid superficial velocities (0.071–0.884 m/s). The experimental conditions were selected based on the flow pattern maps to specifically target stratified and intermittent flows, as shown in Fig. 4, where the conditions were superimposed on the flow pattern maps suggested by Mandhane et al. (1974) and Taitel and Dukler (1976). Within the tested parameter range, two dominant flow patterns were identified: stratified and intermittent (encompassing slug and plug flows). These patterns were prioritized because of their prevalence in industrial pipelines and typical pressure drop mechanisms.

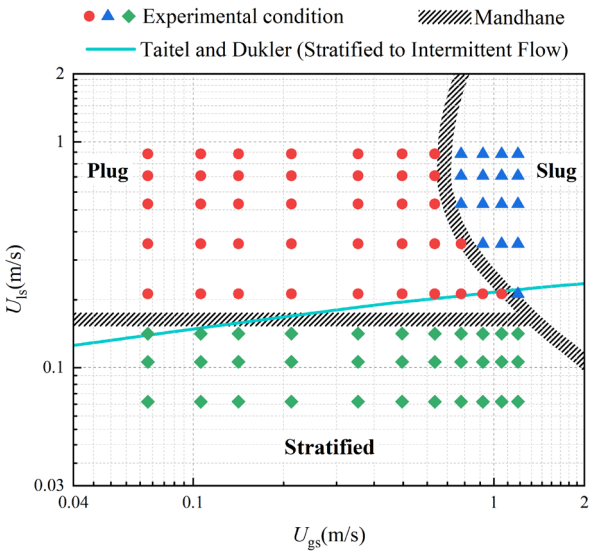

Fig. 4 Two-phase experimental conditions and flow pattern map

2.2 CFD Simulation Model

A three-dimensional CFD simulation model was established based on the geometric dimensions of the contraction pipe used in the experiments. The inlet and outlet pipe lengths were specified as 1.5 m ($15D_1$) and 2 m ($40D_2$), respectively. These dimensions ensured fully developed flow conditions while minimizing boundary effects.

Mesh quality critically determines simulation accuracy and computational efficiency. The entire computational domain was discretized using an O-block-structured mesh division in ANSYS ICEM. High orthogonality was achieved through structured grids that ensured cell alignment along the flow direction, effectively minimizing numerical diffusion and enhancing the accuracy in capturing velocity gradients near the contraction. The controlled cell distribution was maintained by aligning grid lines with the pipe geometry, enabling smooth transitions between regions of varying curvature, such as the contraction inlet/outlet interfaces. The association between the block edges and curves is shown in Fig. 5.

To satisfy the requirements of the turbulence model and wall functions on the mesh quality, we implemented a

Table 2 Information and error of different mesh schemes

NO.	Number of cells				Δp_c (Pa)		Error (%)
	l_1	l_2	Axial	Total	CFD	Experiment	
1	12	8	121	63840	2472.3	2368.0	4.40
2	15	10	188	154660	2414.5		1.96
3	18	13	338	426300	2396.8		1.22
4	20	16	596	1001210	2400.5		1.37
5	22	17	962	1904760	2391.1		0.98
6	24	19	1136	2725810	2389.3		0.90

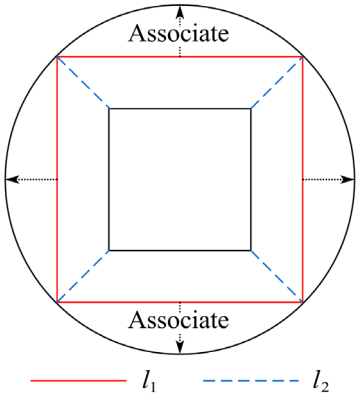

Fig. 5 Association between block edge and curve in O-block

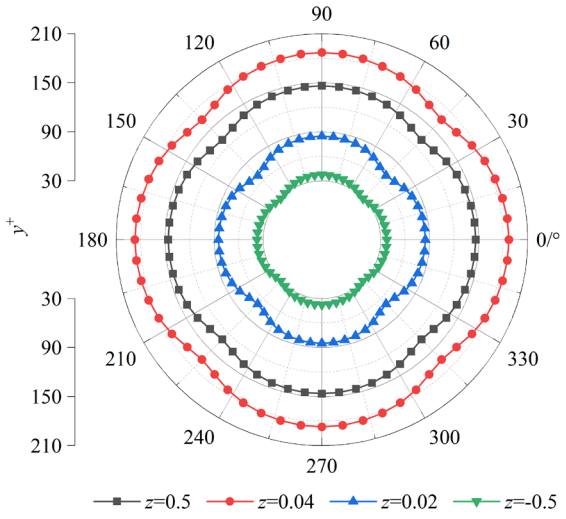

Fig. 6 y^+ value in the circumferential direction

boundary layer mesh with a thickness of 1×10^{-4} m and growth rate of 1.1 near the wall. The standard wall function was adopted after confirming that the y^+ values (30-300) aligned with the wall function applicability range, achieving a balance between near-wall resolution accuracy and computational efficiency. Figure 6 demonstrates the y^+ distribution at different cross sections. This approach avoided excessive mesh refinement while maintaining adequate accuracy.

To check the mesh independence, we adopted six different schemes for mesh independence validation, as shown in Table 2. During independence validation, the pressure drop Δp_c at a single-phase liquid flow rate of $V=$ 15 m^3/h was simulated for different mesh schemes and compared with the corresponding experimental results. Schemes 5 and 6 demonstrated optimal accuracy with error margins below 1% in the validation test. Considering the computational cost, Scheme 5, which contained 1,904,760 cells, was selected for subsequent calculations. The specific numerical mesh for Scheme 5 is shown in Fig. 7.

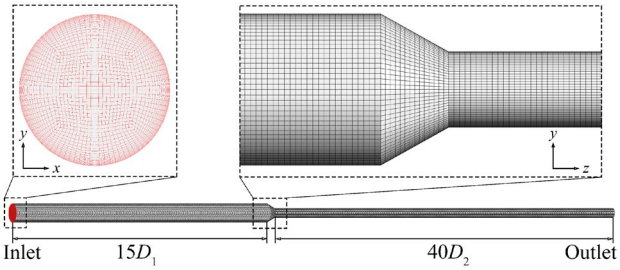

Fig. 7 Numerical mesh

The computational mesh adhered to rigorous quality criteria, achieving a minimum element quality factor of 0.7 through O-block structuring to reduce the velocity gradient discretization errors. Cell isotropy was ensured by maintaining aspect ratios below 5 and skewness values below 0.4, whereas Jacobian determinants exceeding 0.7 prevented element inversion throughout the domain.

The interfacial dynamics and phase distribution in a two-phase system were resolved using the VOF method, which is a widely validated computational technique developed by Hirt and Nichols (1981) to track immiscible fluid interfaces in multiphase flow simulations. The method uses a fluid volume function α to characterize the proportion of the target fluid volume within a cell to the volume of that cell. When α is 1, the cell is fully occupied by target fluid; when it is 0, the cell contains no target fluid; and when it is between 0 and 1, the cell contains an interface between phases and satisfies the following constraints:

$$\sum_{q=1}^{n}\alpha_q = 1 \tag{2}$$

The control equation for the q^{th} phase is

$$\frac{1}{\rho_q}\frac{\partial}{\partial t}\left(\alpha_q\rho_q\right)+\frac{1}{\rho_q}\nabla\cdot\left(\alpha_q\rho_q\vec{\upsilon_q}\right)=\frac{S_{\alpha_q}}{\rho_q}+\frac{1}{\rho_q}\sum_{p=1}^{n}\left(m_{pq}-m_{qp}\right) \tag{3}$$

where α_q is the volume fraction of the q^{th} phase, ρ_q is the density of the q^{th} phase, υ_q is the velocity of the q^{th} phase,

S_{α_q} is the source term of the q^{th} phase, and m_{pq} and m_{qp} denote the mass transfers between the p^{th} and q^{th} phases, respectively.

To ensure physical fidelity, we specified the material properties according to standard atmospheric conditions: the liquid phase (water) was assigned a density of 998 kg/m^3 and dynamic viscosity of 1.01×10^{-3} Pa·s, whereas the gas phase (air) had a density of 1.29 kg/m^3 and dynamic viscosity of 18.1×10^{-6} Pa·s. The interfacial surface tension effects at the gas–liquid interface were explicitly resolved using the continuum surface force (CSF) model proposed by Brackbill et al. (1992), which incorporates surface tension as a volumetric force term in the momentum equations. In this implementation, the CSF model prescribed a constant surface tension coefficient of 0.072 N/m, which corresponded to the experimentally measured interfacial tension value for purified air–water systems under standard conditions. The model formulation converts the surface tension forces into equivalent volume forces distributed across the interface region, enabling their direct integration into the governing momentum equations for the numerical solution.

For pipe flow, the *k*-*ε* family of turbulence models has been shown to provide greater accuracy and veracity. The Realizable *k*-*ε* turbulence model was adopted to resolve the high-strain-rate flow in the contraction of the gas–liquid two-phase flow. It provides improved accuracy for flows involving strong shear and streamline curvature, such as those near the contraction segment, compared with the standard *k*-*ε* model. This balances the computational efficiency and robustness of industrial-scale simulations, as validated in previous studies on pipe contraction. The transport equations corresponding to turbulent kinetic energy k and turbulent dissipation rate ε in the Realizable *k*-*ε* model are as shown in Eqs. (4) and (5), respectively:

$$\frac{\partial(\rho k)}{\partial t}+\frac{\partial(\rho k u_j)}{\partial x_j}=\frac{\partial}{\partial x_j}[(\mu+\frac{\mu_t}{\sigma_k})\frac{\partial k}{\partial x_j}] +G_k+G_b-\rho\varepsilon-Y_M+S_k \tag{4}$$

$$\frac{\partial(\rho \varepsilon)}{\partial t}+\frac{\partial(\rho \varepsilon u_j)}{\partial x_j}=\frac{\partial}{\partial x_j}[(\mu+\frac{\mu_t}{\sigma_\varepsilon})\frac{\partial \varepsilon}{\partial x_j}] +\rho C_1 S\varepsilon-\rho C_2\frac{\varepsilon^2}{k+\sqrt{v\varepsilon}}+C_{1\varepsilon}\frac{\varepsilon}{k}C_{3\varepsilon}P_b+S_\varepsilon \tag{5}$$

where:

$$C_1=\max\left[0.43,\frac{\eta}{\eta+5}\right] \tag{6}$$

$$\eta=\sqrt{2S_{ij}S_{ij}}\frac{k}{\varepsilon} \tag{7}$$

In these equations, G_k represents the turbulent kinetic energy generated by the mean velocity gradient, G_b represents the turbulent kinetic energy generated by buoyancy effects, Y_M represents the influence of fluctuating dilatation in compressible turbulence on the total dissipation rate, σ_k and σ_ε are the Prandtl numbers for k and ε, respectively, S_k and S_ε are source terms, and C_2, $C_{1\varepsilon}$, and $C_{3\varepsilon}$ are constant terms.

The gravitational acceleration was set to 9.81 m/s^2 and directed along the negative y-axis. For the pressure-based transient solver, the Semi-Implicit Method for Pressure-Linked Equations Consistent (SIMPLEC) algorithm was employed for pressure–velocity coupling. The Quadratic Upstream Interpolation for Convective Kinematics (QUICK) scheme was applied for the discretization of the momentum and turbulence terms, whereas the PRESTO! scheme was used for pressure discretization.

No-slip wall boundary conditions were imposed. The velocity inlet and pressure outlet were selected based on the incompressible flow assumption, which was validated by the low Mach number of the system, with all simulated cases exhibiting maximum Mach numbers significantly below 0.3 (peaking at merely 0.06), where the density variations remained below 1%. This configuration enabled the flow conditions at the inlet boundary to be uniquely determined by the gas–liquid flow rate and gas volume fraction. The inlet velocity was calculated by dividing the total volume flow rate by the inlet cross-sectional area to simulate the uniform velocity of the gas–liquid phase fluid exiting the gas–liquid mixer. The inlet gas volume fraction was defined as the ratio of gas flow rate to the total flow rate (β). To balance numerical accuracy with computational economy, we implemented an adaptive temporal discretization scheme, constrained by a minimum time step of 1×10^{-6} s to maintain solution stability while achieving optimal convergence behavior.

3. RESULTS AND DISCUSSION

The aforementioned experimental setup and CFD model were employed to investigate both the single-phase and two-phase flow behaviors under various operating conditions. A comprehensive analysis of the experimental measurements and numerical simulations revealed the distinct pressure drops and flow characteristics of each pattern.

3.1 Pressure Drop and Flow Characteristics of Single-Phase Flow

The single-phase flow in a contraction pipe is a relatively straightforward phenomenon. Consequently, most of the early studies on two-phase pressure drops were based on the assumption of a single-phase flow. In the context of a single-phase liquid flow, the contraction pressure drop is typically expressed as the product of the pressure loss coefficient K_c and the kinetic energy of the flow:

$$\Delta p_c=K_c\frac{G_2^2}{2\rho_L}=\frac{G_2^2}{2\rho_L}\left[\left(C_c^{-1}-1\right)^2+\left(1-\sigma_A^2\right)\right] \tag{8}$$

where G_2 is the mass flow rate of the fluid at the outlet pipe, ρ_L denotes the liquid density, and C_c is the contraction coefficient.

The numerical simulation and experimental results for the single-phase liquid flow are listed in Table 3. The experimental values agreed closely with the simulation results because the pressure drop increased consistently as the volumetric flow rate increased. Minor discrepancies

Table 3 Single-phase Δp_c of experiment and CFD under different volumetric flow rates

V (m³/h)	Δp_c (Pa)		Error (%)
	Experiment	CFD	
2	42.03	44.59	6.09%
3	95.85	95.62	0.24%
4	172.54	170.83	0.99%
6	386.68	384.75	0.50%
10	1036.56	1067.11	2.95%
15	2368.09	2394.14	1.10%
20	4480.92	4243.36	5.30%
25	6812.31	6625.64	2.74%

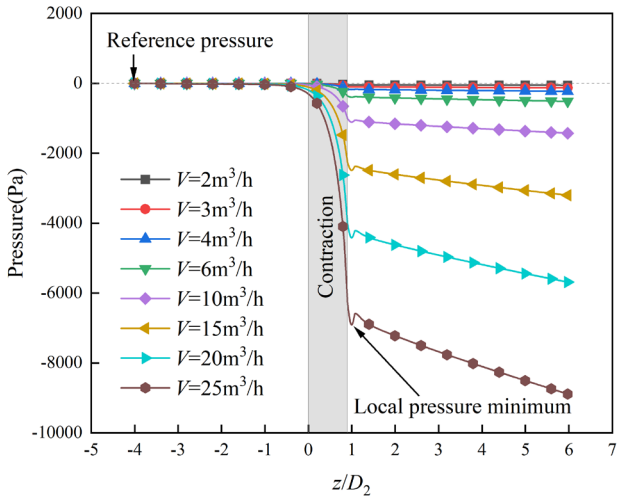

Fig. 8 Pressure profiles of single-phase flow under different volumetric flow rates

between the two methods may have originated from inherent error sources, such as turbulence model limitations in the simulations and experimental uncertainties associated with the flow rate and pressure measurements.

Based on the experimental data, the contraction coefficient C_c was inversely calculated, yielding the contraction coefficient $C_{c,single} = 0.717$ under single-phase flow conditions, which was greater than the theoretical prediction of the Chisholm correlation (Eq. (9); Chisholm, 1985) and the Geiger correlation (Eq. (10); Geiger, 1964) for sudden contractions with the same area ratio. Its smaller degree of vena contracta and lower pressure loss were demonstrated and applied in further calculations.

$$C_c = \frac{1}{0.639\left(1-\sigma_A\right)^{0.5}+1} \tag{9}$$

$$C_c = 1-\frac{1-\sigma_A}{2.08\left(1-\sigma_A\right)+0.5371} \tag{10}$$

The CFD simulation results revealed the axial pressure distribution characteristics of the single-phase flows across the volumetric flow rates, as shown in Fig. 8. A persistent local pressure minimum was observed $0.12D_2$ downstream of the contraction exit. This position can be considered as the location of the vena contracta point, indicating vena contracta formation in a single-phase

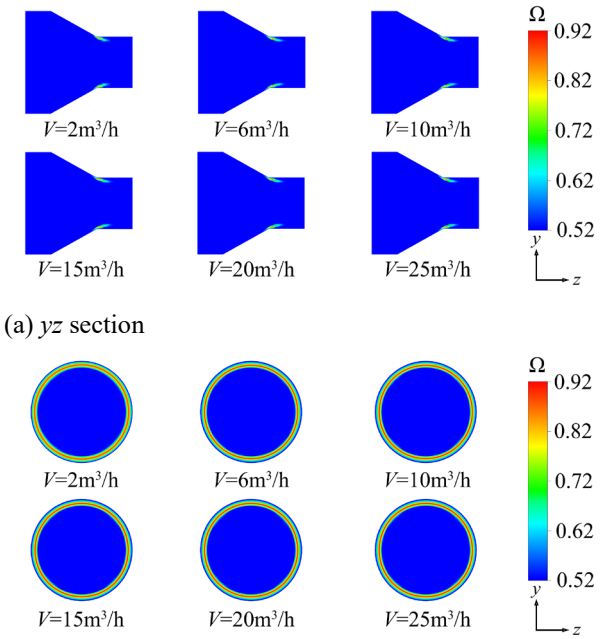

(a) *yz* section

(b) vena contracta section

Fig. 9 Ω contours of single-phase flow under different volumetric flow rates

flow. The formation mechanism of the local minimum pressure is closely related to the flow characteristics of the fluid from the vena contracta point to the fully developed region downstream, a process analogous to the flow in sudden expansion, as described by Song et al. (2023).

In subsequent studies on flow characteristics, the Ω vortex identification method was employed to analyze the eddies and vena contracta phenomenon within the contraction pipe. This method is not subject to the subjective selection of thresholds (Zhang et al., 2019). According to Liu et al. (2019; 2016), a fixed threshold of Ω = 0.52 is commonly adopted in practical applications to identify eddy zones.

The Ω contours of the single-phase flow in the contraction pipe under different volumetric flow rates are plotted in Fig. 9. The results demonstrated that the distribution characteristics of the eddy zones under various volumetric flow rates were highly consistent. This suggests that the flow rate had a negligible influence on the eddy distribution and vena contracta. Figure 9(a) shows the flow separation of the fluid from the pipe wall at the exit of the contraction segment, which resulted in the formation of an eddy zone. The measured length of the eddy zone was approximately $0.37D_2$. Furthermore, Fig. 9(b) shows that the eddy zone caused by the single-phase flow separation from the pipe wall exhibited axial symmetry along the central axis and a uniform circumferential distribution at the front end of the outlet pipe.

3.2 Pressure Drop and Flow Characteristics of Two-phase Flow

The experimental results established the relationship between the two-phase contraction pressure drop Δp_c and flow quality x under varying liquid superficial velocities

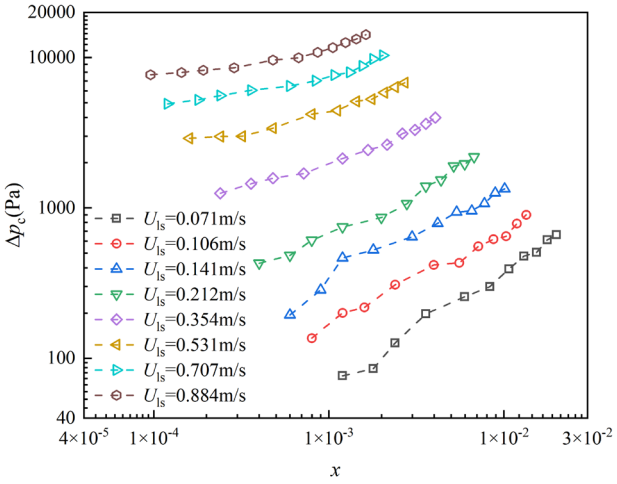

Fig. 10 Variation of two-phase Δp_c with flow quality under different liquid superficial velocities

U_{ls}, as shown in Fig. 10. At a constant liquid superficial velocity, the pressure drop increased with increasing flow quality owing to gas-phase flow augmentation. Conversely, at a fixed gas-phase flow rate, an increased liquid superficial velocity reduced the flow quality but increased the pressure drop through an enhanced mass flow rate dominated by the liquid-phase density.

To reveal the differences in the pressure drop characteristics between the two- and single-phase flows, we conducted a CFD simulation to analyze the axial pressure distributions of the stratified two-phase flows under varying gas and liquid superficial velocities, as shown in Fig. 11. The axial pressure curves of the stratified flows lacked a local minimum pressure point, indicating the absence of vena contracta. This observation was consistent with the findings of Schmidt and Friedel (1997). The pressure distribution in the stratified flow revealed fundamental differences in the flow behavior compared with those in single-phase flows.

The experimentally measured data of the two-phase pressure drop were comparatively analyzed using four existing pressure drop prediction models: the homogeneous flow model, Schmidt and Friedel correlation (Schmidt & Friedel, 1997), Padilla correlation (Padilla et al., 2013), and Abdelall correlation (Abdelall et al., 2005). The homogeneous flow model is defined by Eq. (11), and the specific expressions of the Schmidt, Padilla, and Abdelall correlations are provided in the Appendix.

$$\Delta p_c = \frac{G_2^2}{2\rho_L}\left[\left(C_c^{-1}-1\right)^2+\left(1-\sigma_A^2\right)\right]\left[1+x\left(\frac{\rho_L}{\rho_G}-1\right)\right] \tag{11}$$

where x is the flow quality, ρ_G is the gas density, and C_c is the contraction coefficient, with $C_{c,single} = 0.717$ used in the calculations based on the single-phase flow experimental results. The definitions of the mean absolute error (MAE) and mean relative error (MRE) are given in Eqs. (12) and (13), respectively:

$$\mathrm{MAE}=\frac{1}{n}\sum_{i=1}^{n}\left|\frac{X_i^e - X_i^m}{X_i^m}\right| \tag{12}$$

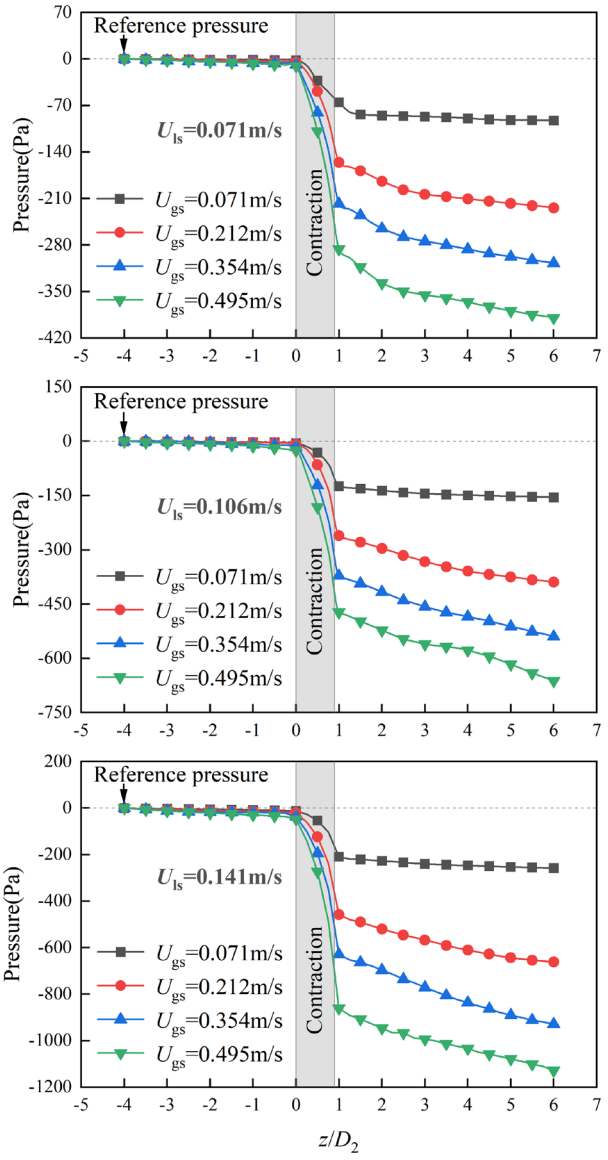

Fig. 11 Pressure profiles of two-phase flow under different gas and liquid superficial velocities

$$\mathrm{MRE}=\frac{1}{n}\sum_{i=1}^{n}\left(\frac{X_i^e - X_i^m}{X_i^m}\right) \tag{13}$$

where X^e represents the experimental data, and X^m represents the data calculated by the model. The ±30% error band indicates the proportion of data points for which the error lay within ±30% of the total data points.

By comparing the experimental two-phase flow pressure-drop data consisting of 88 data points with the four aforementioned pressure-drop prediction models, we analyzed the predictive performance and error of each model, as shown in Fig. 12. The results demonstrated that both the homogeneous flow model and Schmidt correlation achieved lower MAEs in the two-phase pressure drop predictions, whereas the Schmidt correlation demonstrated higher precision in terms of the MRE. However, the Schmidt correlation relies on more than 15 empirical coefficients during the calculations, some of which were not defined at the physical limits. Notably, both the homogeneous flow model and Padilla

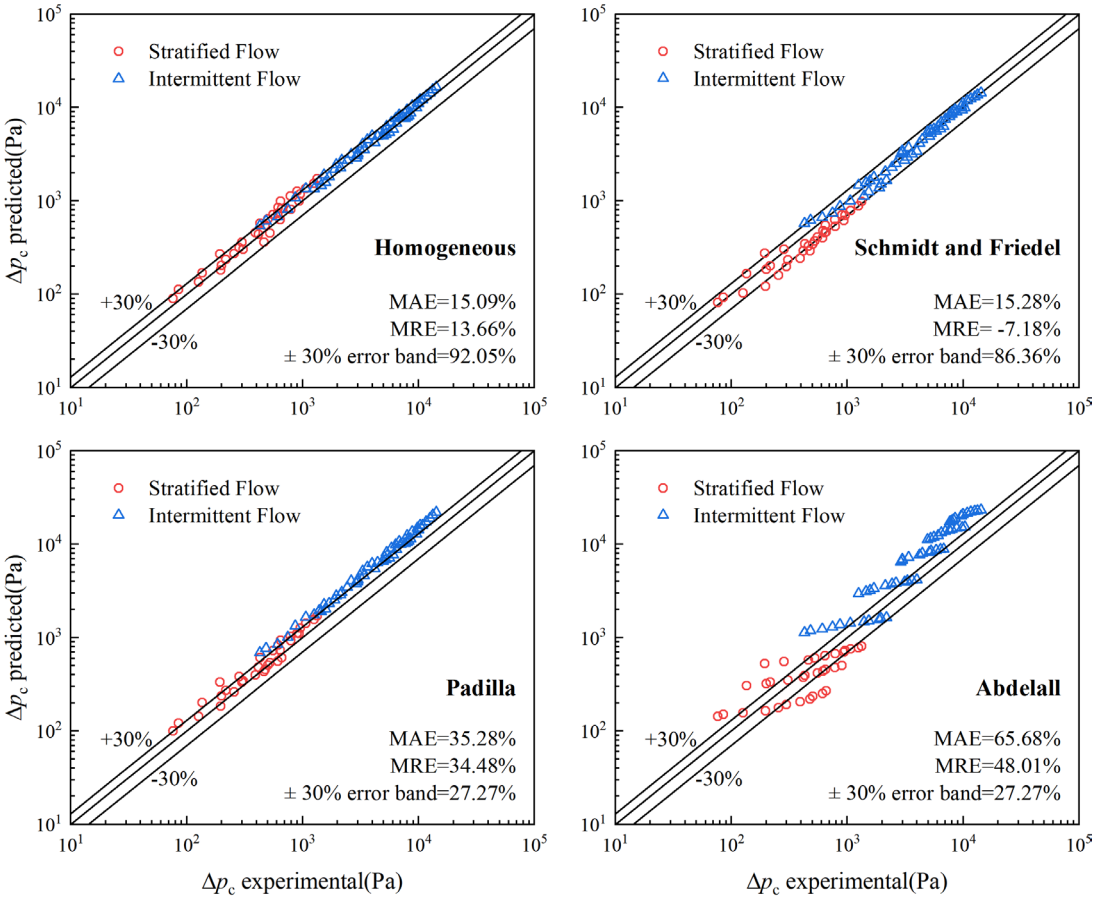

Fig. 12 Comparison between the experimental data and the existing models

correlation overpredicted values, with the Padilla correlation exhibiting acceptable accuracy (±30% error) for only 24 of the 88 data points (27.27%). The Abdelall correlation performed the least favorably, exhibiting 30%–50% higher MAE values than the other models. This inferior performance could be attributed to the foundational assumption of minimum entropy production derived from an idealized annular flow, which led to an overestimated slip ratio under conditions of low gas-phase volume fractions.

The two-phase multiplier Φ^2 quantifies the relationship between the two- and single-phase pressure drops. For the liquid-phase analysis, this multiplier is subdivided into two distinct parameters: liquid-only multiplier Φ_{LO}^2 and all-liquid multiplier Φ_L^2. The liquid-only multiplier is mathematically defined as

$$\Phi_{LO}^2 = \frac{\Delta p_{TP}}{\Delta p_{LO}} \tag{14}$$

where Δp_{TP} denotes the pressure drop experienced in a two-phase flow through the pipe, and Δp_{LO} denotes the pressure drop when the liquid phase flows through an identical pipe alone.

The liquid-only multiplier Φ_{LO}^2 can be determined analytically using the Chisholm correlation (Chisholm, 1985):

$$\Phi_{LO}^2 = 1 + \frac{C}{X} + \frac{1}{X^2} \tag{15}$$

where the empirical coefficient C depends on the flow regime. C = 20 for both gas and liquid phases under turbulent conditions. The Martinelli parameter X is defined as

$$X = \left(\frac{1-x}{x}\right)^{0.9} \left(\frac{\mu_L}{\mu_G}\right)^{0.1} \left(\frac{\rho_G}{\rho_L}\right)^{0.5} \tag{16}$$

The two-phase pressure drop data were analyzed by calculating the ratio of each experimental value to the corresponding single-phase pressure drop. This approach quantified the relationship between the liquid-only multiplier Φ_{LO}^2 and flow quality x, as shown in Fig. 13. The results demonstrated that the multiplier increased with flow quality yet remained independent of variations in the mass flow rate. Notably, the multiplier converged to 1 for a sufficiently low flow quality ($\Phi_{LO}^2 \to 1$ as $x \to 0$), confirming the physical continuity between the two- and single-phase flows. Furthermore, the experimental data aligned well with the trend predicted by the Chisholm correlation, demonstrating high consistency.

3.3 Influence and Mechanism of Flow Pattern on Two-Phase Contraction Pressure Drop

To investigate the effect of the two-phase flow patterns in the contraction pipe on the pressure drop and

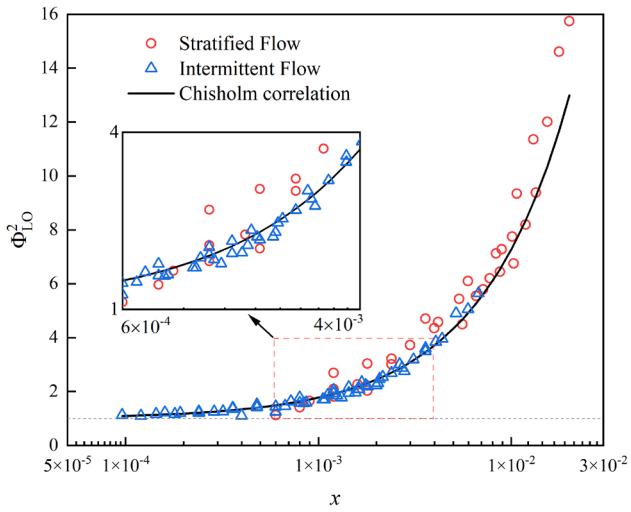

Fig. 13 Comparison of experimental Φ_{LO}^2 with Chisholm correlation

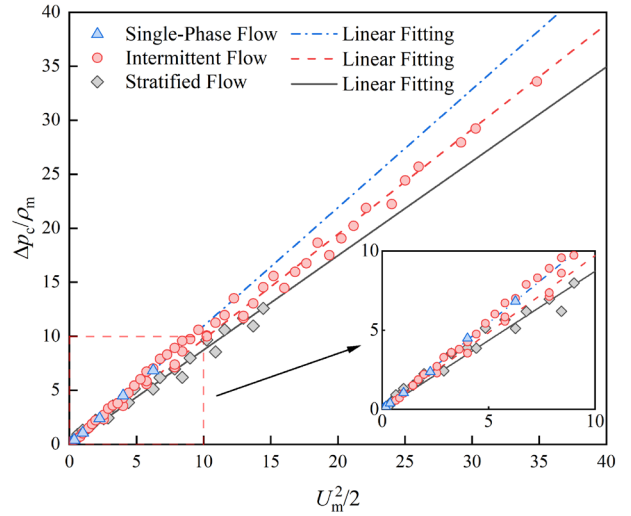

Fig. 14 Variation of $\Delta p_c/\rho_m$ with $U_m^2/2$ across flow patterns and linear fitting

its mechanism, we examined the pressure loss coefficient K_c for both the two-phase and single-phase flows under different flow patterns. The pressure loss h_f in the two-phase flow caused by the contraction pipe can be expressed as

$$h_f = \frac{\Delta p_c}{\rho_m} = K_c \frac{U_m^2}{2} \tag{17}$$

where ρ_m represents the mean density of the two-phase flow, which is related to the volumetric gas fraction β of the two-phase flow and is defined as $\rho_m = \beta\rho_G + (1-\beta)\rho_L$. U_m represents the mean velocity of the two-phase flow, $U_m = U_{ls} + U_{gs}$.

The experimental measurements established functional relationships between $\Delta p_c/\rho_m$ and $U_m^2/2$ for both single- and two-phase flows, with linear regression analysis applied to each dataset (considering the single-phase flow as the limiting case of zero gas content), as

Table 4 K_c corresponding to different flow patterns

Flow patterns	K_c
Stratified flow	0.873
Intermittent flow	0.972
Single-phase flow	1.095

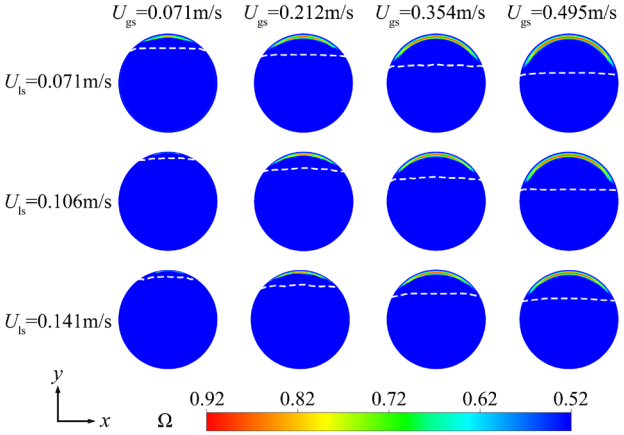

Fig. 15 Ω contours of stratified flow under different gas and liquid superficial velocities

presented in Fig. 14. The regression slopes quantitatively represent the pressure loss coefficient, K_c, which characterizes each flow pattern. A comparative analysis revealed distinct K_c magnitudes across the flow patterns; single-phase flow demonstrated the maximum coefficient value, stratified flow the minimum, and intermittent flow fell between the two. The specific values of K_c for each flow pattern are listed in Table 4.

To further reveal the influence of the flow patterns in the contraction pipe on the pressure-drop characteristics, we analyzed numerical simulation results to investigate the flow behavior of different two-phase flow patterns and explore the key factors affecting the pressure drop and vena contracta.

Figure 15 plots the Ω contours at the vena contracta section for stratified flow under varying gas and liquid superficial velocities, with the dashed lines denoting phase interfaces. The eddy distribution fundamentally differed from that of the single-phase flow, with eddies solely restricted to the gas phase above the interface and no vortex formation in the liquid phase. At the minimum void fraction (U_{ls} = 0.141 m/s and U_{gs} =0.071 m/s), the gas-phase eddies exhibited the smallest spatial extent and weakest intensity. As U_{gs} increased or U_{ls} decreased, the interface progressively lowered, whereas the gas-phase eddy zone expanded circumferentially, resembling single-phase flow distribution patterns. This implied that in the contraction pipe stratified flow, the liquid phase, which significantly contributed to the pressure drop, failed to develop eddies as observed in single-phase flow, thereby eliminating the vena contracta effect and its characteristic pressure drop behavior.

To elucidate the interphase interaction mechanisms of the two-phase flow, we analyzed the void fraction evolution for the stratified flow through the contraction

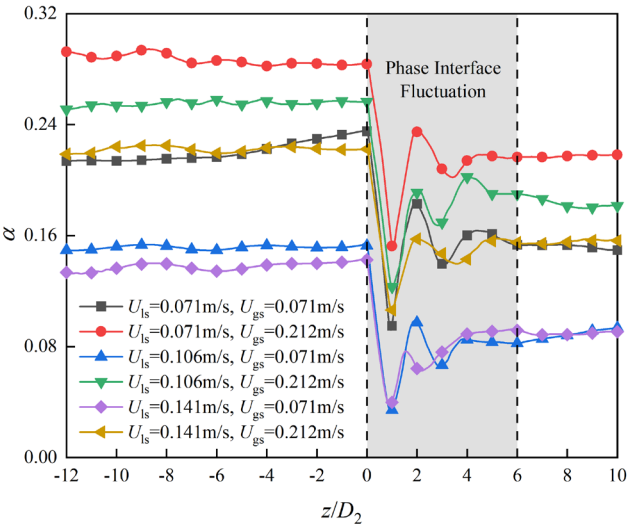

Fig. 16 Variation of void fraction with axial position for stratified flow under different gas and liquid superficial velocities

pipe, as shown in Fig. 16. Three characteristic stages emerged during this evolution. In the inlet region, a stable void fraction distribution was maintained with negligible axial variation, thereby confirming flow-pattern equilibrium. The sudden contraction led to a significant change in the void fraction and the formation of interface fluctuations. According to the relationship between the void fraction and slip ratio S in the two-phase flow (Eq. 18), the slip ratio of the two-phase flow S also changed significantly, resulting in a strong exchange of momentum to change the velocity of each phase.

$$\alpha = \left(1 + \frac{(1-x)}{x}\frac{\rho_G}{\rho_L}S\right)^{-1} \tag{18}$$

This stage exhibited pronounced interphase interactions that influenced the flow field, extending from the contraction entrance to approximately $6D_2$ downstream. The gas–liquid interface within the outlet region regained stability as the contraction-induced interfacial fluctuations diminished. These observations demonstrate that phase property disparities lead to significant interphase interactions during contraction, resulting in distinct flow characteristics compared with single-phase flow and fundamentally affecting the flow behavior and pressure drop mechanisms.

In studies on intermittent flows, the flow characteristics of the gas and liquid phases differ significantly from those of continuous flows, manifesting as periodic or stochastic alternations between liquid slugs and gas bubbles. Under this flow pattern, the liquid slug and liquid film regions exhibit distinct flow behaviors as they transit through the contraction segment. To investigate the transient behavior of intermittent flow in the contraction pipe, we applied periodic boundary conditions to the liquid-phase fraction at the pipe inlet by utilizing the user-defined function (UDF) capability, which simulated the intermittent flow pattern.

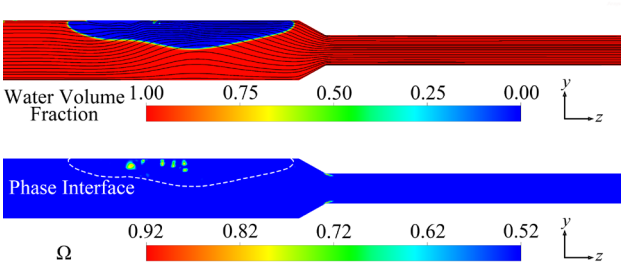

(a) Transit of liquid slug region through the contraction segment

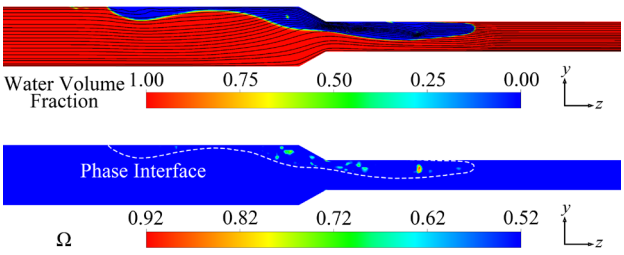

(b) Transit of liquid film region through the contraction segment

Fig. 17 Intermittent flow in the contraction pipe

The intermittent flow in the contraction pipe was analyzed through a numerical simulation, and the corresponding flow characteristics are presented in Fig. 17. During the transit of the liquid slug through the contraction segment, eddy zones resembling those in single-phase flow were observed downstream, as shown in Fig. 17(a). This observation suggested that the contraction segment was predominantly occupied by a single liquid phase during liquid slug transit, with flow separation characteristics analogous to a single-phase flow, which induced the vena contracta phenomenon.

During the transit of the liquid film region through the contraction segment, the Ω contour demonstrated that the gas-phase fluid within the gas bubble separated from the wall and formed eddies that were weaker than those formed during the liquid slug transit. Moreover, no distinct eddy zones emerged in the liquid film below the gas bubble, as shown in Fig. 17(b). Additionally, the streamline further revealed a behavior similar to that of a stratified flow: the gas–liquid interface protruded upward, and the flow direction differed from the uniform convergence observed when the liquid slug transited.

To further elucidate the transient characteristics of the intermittent flow, we investigated the flow behavior within the contraction pipe by positioning a monitoring surface and point. The monitoring surface was positioned at the exit cross-section of the contraction segment, and the monitoring point was placed at the location at which the Ω value reached its maximum at the bottom of the outlet pipe during the transit of the liquid slugs.

The temporal variations in the void fraction α (cross-section of the monitoring surface) and Ω value (monitoring point) are shown in Fig. 18. During the transit of the liquid slug through the contraction segment, the void fraction remained zero, confirming the complete

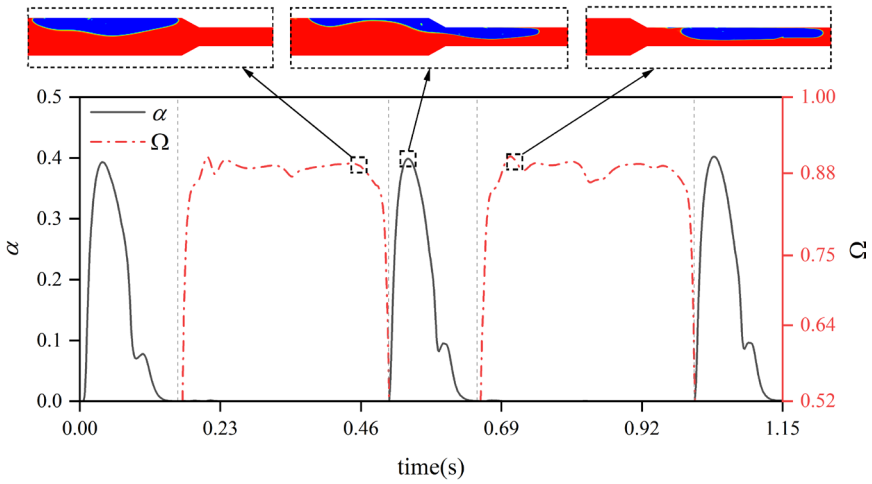

Fig. 18 Temporal variations of α and Ω at the monitoring position

occupation of this segment by the liquid. The Ω value at the monitoring point remained stable, suggesting the formation of stable eddy zones at this position. After the liquid slug fully exited the contraction segment, the gas bubble initiated its transit through this region. At this stage, the void fraction suddenly increased from zero, whereas the Ω value at the monitoring point declined sharply, reflecting the dispersion of the previously stable eddy. Combined with Fig. 17(b), we can infer that the two-phase flow characteristics at this stage resembled those of stratified flow with no significant vena contracta. This indicated that the flow behavior of the gas–liquid phases during the transit of the gas bubble differed significantly from that of the single-phase flow and was in contrast to the flow characteristics observed during the transit of the liquid slug. Therefore, the different flow behaviors of the liquid slug and liquid film regions in the intermittent flow were further revealed.

Numerical investigations of intermittent flow revealed that during gas bubble transit through the contraction segment, interphase interactions between the upper gas bubble and lower liquid film induce a stratified-like flow pattern. Although the gas-phase fluid still separates from the wall with accompanying eddy formation, this interphase interaction effectively suppresses the development of vena contracta. In contrast, when the liquid slug transits through the contraction segment, because it is predominantly a single-phase liquid, its flow behavior resembles that of single-phase conditions, enabling the formation of vena contracta.

Consequently, the intermittent flow manifests as a hybrid flow behavior, integrating the features of single-phase and stratified flows, wherein vena contracta formation occurs intermittently during the flow process. These flow features significantly affect the predictive accuracy of the two-phase-flow pressure drop across the contraction pipe. For reliable pressure-drop predictions in contraction pipes, transient vena contracta effects induced by liquid slugs should be explicitly incorporated into the pressure-drop model.

4. IMPROVED PREDICTION MODEL OF CONTRACTION PRESSURE DROP

The combined experimental and numerical results demonstrated that single-phase, stratified, and intermittent flows exhibited distinct pressure-drop behaviors in the contraction segment. Notably, stratified flow showed negligible vena contracta effects, which justified the exclusion of this phenomenon from the corresponding predictive models:

$$C_{\text{c, stratified}} = 1 \tag{19}$$

The liquid slug and adjacent liquid film regions constitute an intermittent unit. The preceding analysis reveals that in an intermittent flow, the vena contracta develops exclusively during liquid slug transit through the contraction segments. Therefore, the average contraction coefficient for the intermittent flow can be derived by determining the fractions of the liquid slug and liquid film regions in the intermittent flow as follows:

$$\begin{aligned} C_{\text{c, intermittent}} &= f_{\text{s}} \cdot C_{\text{c,single}} + (1 - f_{\text{s}}) \cdot C_{\text{c, stratified}} \\ &= f_{\text{s}} \cdot C_{\text{c,single}} + (1 - f_{\text{s}}) \cdot 1 \end{aligned} \tag{20}$$

where f_{s} represents the liquid slug fraction and denotes the length proportion of the liquid slug within an intermittent unit:

$$f_{\text{s}} = \frac{L_{\text{s}}}{L_{\text{s}} + L_{\text{f}}} \tag{21}$$

where L_{s} and L_{f} represent the lengths of the liquid slug and film regions, respectively, as shown in Fig. 19(a).

Based on the assumptions of the homogeneous flow model, the proportions of gas and liquid phases in an intermittent unit can be derived directly as the ratio of their volumetric flow rates:

$$\frac{v_{\text{G}}}{v_{\text{L}}} = \frac{L_{\text{f}}(1 - \alpha_{\text{f}})}{L_{\text{s}} + L_{\text{f}} \cdot \alpha_{\text{f}}} = \frac{V_{\text{G}}}{V_{\text{L}}} = \frac{\beta}{1 - \beta} \tag{22}$$

where v_{G} and v_{L} denote the volumes occupied by the gas

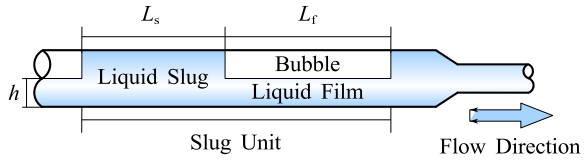

(a) Intermittent flow model

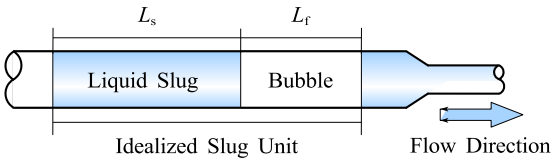

(b) Idealized intermittent flow model

Fig. 19 Intermittent flow and its idealized model

and liquid phases within an intermittent unit, respectively, and α_f represents the ratio between the liquid film cross-sectional area in the liquid film region and pipe cross-sectional area. The liquid film height beneath a gas bubble is defined as h, which satisfies the following condition:

$$\alpha_f = \frac{1}{\pi}\left[\arccos\left(1-\frac{2h}{D}\right) - 2\left(1-\frac{2h}{D}\right)\sqrt{\frac{h}{D}-\left(\frac{h}{D}\right)^2}\right] \tag{23}$$

Substituting Eq. (22) into Eq. (21), the liquid slug fraction f_s can be expressed as

$$f_s = \frac{L_s}{L_s + L_f} = 1 - \frac{\beta}{1-\alpha_f} \tag{24}$$

Considering an idealized intermittent flow model, as shown in Fig. 19(b), by neglecting the influence of the liquid film height h on the liquid slug fraction f_s and setting $\alpha_f = 0$ in the calculation, the liquid slug fraction f_s can be simplified as

$$f_s = 1 - \frac{\beta}{1-\alpha_f} = 1 - \beta \tag{25}$$

Substituting Eq. (25) into Eq. (20), the average contraction coefficient for the intermittent flow $C_{c,\,\text{intermittent}}$ can be expressed as

$$C_{c,\,\text{intermittent}} = (1-\beta)\cdot C_{c,\text{single}} + \beta \tag{26}$$

Analysis of the flow pattern map reveals that bubbly flow emerges when the liquid superficial velocity increases beyond the critical values in the intermittent flow. This implies that bubbly flow constitutes the limiting case of intermittent flow, which is characterized by an elevated liquid content and a reduced volumetric gas fraction. Under these conditions, Eq. (26) can be approximately rewritten as

$$C_{c,\text{bubbly}} = C_{c,\text{single}} \tag{27}$$

Hwang and Pal (1997) confirmed that bubbly flow (characterized by small, uniformly distributed bubbles) can be modeled as a pseudo-homogeneous fluid with effective average properties. Their measurements showed that the pressure loss coefficient in the contraction pipe for a bubbly flow matches the single-phase flow values. This equivalence implies that the bubbly flow exhibits a single-phase-like behavior, enabling the vena contracta phenomenon to develop.

Analogous to stratified flow, annular flow exhibits interphase interactions between the outer liquid film and inner gas core during pipe contraction, which influences the formation of the vena contracta. The experimental results of Schmidt and Friedel (1997) corroborated this conclusion. This suggests that annular flow shares the same inability as stratified flow in developing vena contracta:

$$C_{c,\,\text{annular}} = 1 \tag{28}$$

Substituting the contraction coefficients in Eqs. (19), (26), (27), and (28) for stratified, intermittent, bubbly, and annular flows, respectively, into a homogeneous flow model, Eq. (11), the following equation is obtained:

$$\Delta p_c = \frac{G_2^2}{2\rho_L}\left[\left(C_{c,\text{modify}}^{-1}-1\right)^2 + \left(1-\sigma_A^2\right)\right]\left[1 + x\left(\frac{\rho_L}{\rho_G}-1\right)\right] \tag{29}$$

where $C_{c,\text{modify}}$ is determined by the inlet flow pattern:

$$C_{c,\text{modify}} = \begin{cases} C_{c,\text{single}}, & \text{for bubbly flow} \\ (1-\beta)\cdot C_{c,\text{single}} + \beta, & \text{for intermittent flow} \\ 1, & \text{for other flow patterns} \end{cases} \tag{30}$$

Equation (30) shows that the vena contracta induced by liquid slugs causes the intermittent flow to maintain a lower average contraction coefficient than that of the stratified flow. This flow characteristic predicts pressure loss coefficients that surpass those of the stratified flow. The experimental data presented in Table 4 validate this theoretical prediction through quantitative analysis.

Figure 20 presents a comparative analysis of the experimental pressure drop data for intermittent flow evaluated against three models: the homogeneous flow model, vena contracta exclusion model (C_c = 1), and improved model. The results revealed that under low-flow quality conditions, omission of the vena contracta causes significant prediction errors. This error is attributed to the higher liquid slug fractions under low gas flow rates, where the vena contracta effects account for a significant portion of the total pressure drop calculations. As the flow quality approaches the vanishing limit, the two-phase flow pattern transitions to single-phase characteristics, whereas the improved model includes a description of this transition ($C_{c,\text{intermittent}} \to C_{c,\text{single}}$ as $x \to 0$). Furthermore, under constant U_{ls} conditions, an increased gas flow rate results in a deterioration in the accuracy of the homogeneous flow model. This deviation occurs because the liquid slug fraction decreases with an increase in the gas flow rate, whereas the homogeneous flow model neglects the influence of gas flow rate variations on the contraction coefficient in intermittent flow.

Therefore, the gas flow rate exhibits two opposing effects on the pressure drop characteristics of intermittent flow. Primarily, elevated gas flow rates amplify the mass flow rate and quality of the two-phase flow, thereby

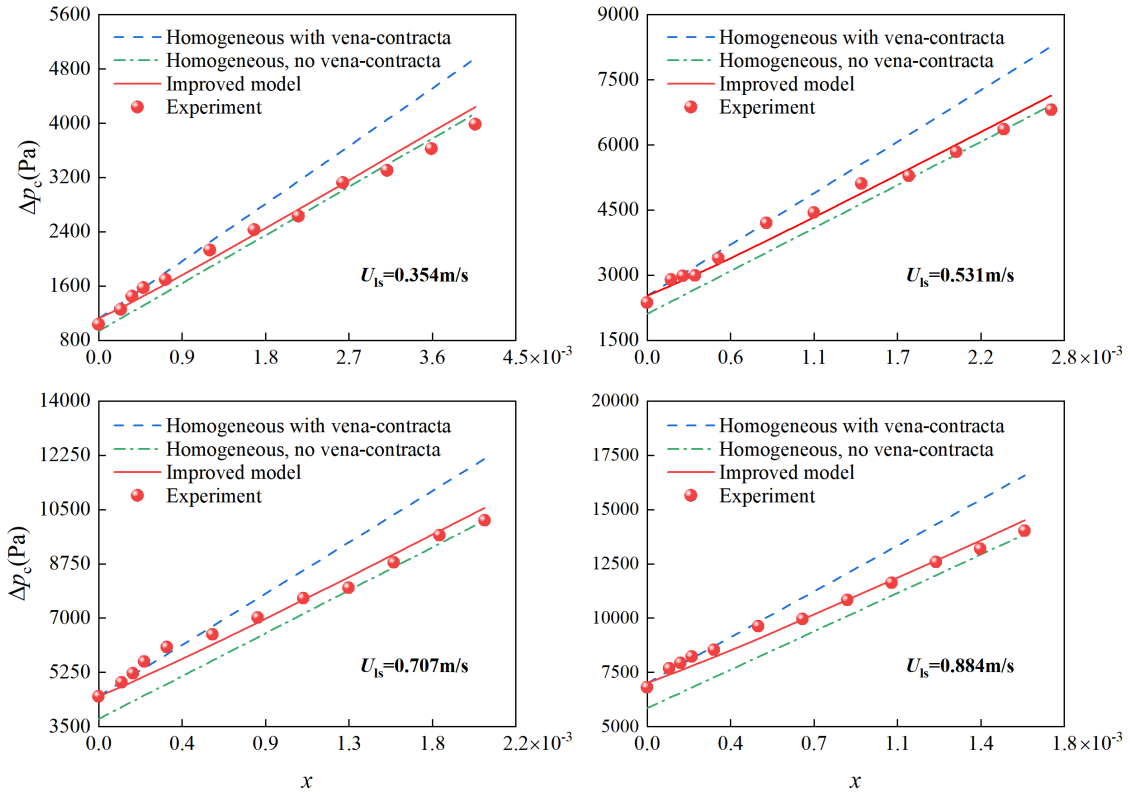

Fig. 20 Comparison of experimental data and improved models in intermittent flow

Table 5 Comparison of errors between the improved model and the homogeneous flow model

	Homogeneous	Improved model
MAE	15.09%	7.03%
MRE	13.66%	1.14%
±20% error band	68.18%	95.45%
±10% error band	38.64%	76.14%

increasing the magnitude of the pressure drop. Conversely, under a constant liquid flow rate, an increase in the gas flow rate results in a decrease in the liquid slug fraction f_s in the intermittent flow, thereby reducing the pressure drop.

As shown in Table 5, a comparative analysis of the experimental two-phase pressure-drop data was conducted to assess the error metrics and data point distributions of the improved and homogeneous flow models. The improved model demonstrated superior accuracy, as evidenced by its lower MAE and MRE values compared with those of the homogeneous flow model. Specifically, 95% of the predictions were achieved within an error range of 20%. The enhancement in all the error metrics validated the enhanced precision of the improved model, thereby confirming its theoretical validity.

Additionally, as shown in Table 6, a paired *t*-test was conducted to ascertain the statistical significance of the enhancements in the prediction accuracy attained by the improved model. The results of this test yielded a *p*-value of less than 0.001, thereby confirming that the observed

Table 6 Parameters of the paired *t*-test

	$\bar{d}$	s_d	t	p
Value	407.672	465.286	8.172	1.1×10^{-12}

improvements in prediction accuracy were statistically significant.

Furthermore, the vena contracta phenomenon is not exclusive to pipes exhibiting gradual contraction. The sudden contractions and orifice plates exhibit more pronounced vena contracta formation under single-phase flow conditions than under gradual contractions. The vena contracta-induced pressure loss accounts for a substantially larger proportion of the total pressure drop in these configurations. These findings demonstrate the broad applicability of the proposed model to flow systems with sudden contractions and orifice plates. The improved model effectively elucidated the effects of the flow pattern on the contraction pressure drop. Future studies could further validate and extend the applicability of the model by testing it with different fluids, pipe geometries, or flow patterns, thereby refining its robustness across diverse industrial scenarios.

5. CONCLUSION

This study investigated the pressure drop and flow characteristics of single-phase, stratified, and intermittent flows in a horizontal contraction pipe through experimental investigations and CFD simulations. By combining the experimental and numerical results, we analyzed the flow behavior and pressure drop under

different flow patterns in detail from the perspective of the vena contracta phenomenon. Based on these findings, a method for calculating the contraction coefficient in a two-phase flow under different flow patterns was proposed, which improves the homogeneous pressure-drop model. The following conclusions were drawn:

1. The single-phase flow in the contraction pipe induces circumferential eddy zones downstream of the contraction segment owing to abrupt variations in the pipe boundary. This flow characteristic also generates a vena contracta that directly influences the pressure drop.

2. For two-phase flow, different flow patterns exhibited distinct flow characteristics in the contraction pipe. In stratified flow, the gas-phase fluid separates from the pipe wall and forms eddy zones. However, interphase interactions between the gas and liquid phases prevent the liquid-phase fluid (the primary contributor to the contraction pressure drop) from experiencing flow separation. This suppression of the flow separation inhibits the vena contracta phenomenon, thereby reducing its effect on the two-phase pressure drop.

3. The intermittent flow in the contraction pipe exhibited characteristics resembling a hybrid of single-phase and stratified flow patterns. Within the intermittent unit, the liquid slug and liquid film regions exhibited distinct flow behaviors. During liquid slug transit, the liquid phase fully occupies the contraction segment, exhibiting a single-phase-like flow behavior that induces a transient vena contracta phenomenon. Conversely, during gas bubble transit, the gas phase occupies the upper contraction segment, and interphase interactions cause the liquid film region to exhibit a stratified-flow-like behavior that suppresses this phenomenon.

4. In intermittent flow, increasing the gas flow rate exerts two opposing effects. Primarily, the intensified gas flow rate increased both the mass flow rate and quality, consequently exacerbating the contraction pressure drop. Conversely, an increased gas flow rate reduces the liquid slug fraction, which is a characteristic of an intermittent flow. This decrease in slug frequency results in diminished formation of the vena contracta, resulting in attenuation of the contraction pressure drop.

5. By comparing the experimental data with the original and improved pressure drop prediction models, the improved model exhibited a 53% reduction in mean absolute error (from 15.09% to 7.03%) and a 92% decrease in relative mean error (from 13.66% to 1.14%) across 88 experimental data points, with 95% of predictions falling within ±20% error bands compared with only 68% in the original homogeneous flow model. A paired *t*-test comparing the errors of the original and improved models ($t(87) = 8.172, p < 0.001$) confirmed the statistical significance of the accuracy improvement.

ACKNOWLEDGEMENTS

This research did not receive any specific grant from funding agencies in the public, commercial, or not-for-profit sectors.

CONFLICT OF INTEREST

The authors have no conflicts of interests to disclose.

AUTHORS CONTRIBUTION

Jiahao Wen: Conceptualization, Methodology, Software, Experimental Execution, Data Curation, Formal Analysis, Validation, Original Draft; **Yufeng Ren:** Experimental Setup Design and Construction; **Dan Wang:** CFD Methodology Review and Validation; **Changqing Bai:** Resources Provision, Methodological Supervision, Manuscript Review.

REFERENCES

Abdelall, F., Hahn, G., Ghiaasiaan, S., Abdel-Khalik, S., Jeter, S., Yoda, M., & Sadowski, D. (2005). Pressure drop caused by abrupt flow area changes in small channels. *Experimental thermal and fluid science*, *29*(4), 425-434. https://doi.org/10.1016/j.expthermflusci.2004.05.001

Ahmadpour, A., Abadi, S. N. R., & Kouhikamali, R. (2016). Numerical simulation of two-phase gas–liquid flow through gradual expansions/contractions. *International Journal of Multiphase Flow*, *79*, 31-49. https://doi.org/10.1016/j.ijmultiphaseflow.2015.10.008

Akhlaghi, M., Mohammadi, V., Nouri, N. M., Taherkhani, M., & Karimi, M. (2019). Multi-Fluid VoF model assessment to simulate the horizontal air–water intermittent flow. *Chemical Engineering Research and Design*, *152*, 48-59. https://doi.org/10.1016/j.cherd.2019.09.031

Al'Ferov, N., & Shul'Zhenko, Y. N. (1977). Pressure drops in two-phase flows through local resistances. *Fluid Mechanics Soviet Research*, *6*, 20-33.

Amini, Y., Ghazanfari, V., Heydari, M., Shadman, M. M., Khamseh, A. G., Khani, M. H., & Hassanvand, A. (2023). Computational fluid dynamics simulation of two-phase flow patterns in a serpentine microfluidic device. *Scientific Reports*, *13*(1), 9483. https://doi.org/10.1038/s41598-023-36672-6

Attou, A., & Bolle, L. (1995). Evaluation of the two-phase pressure loss across singularities. *ASME-Publications-Fed*, *210*, 121-128.

Beattie, D. R., & Whalley, P. (1982). Simple two-phase frictional pressure drop calculation method. *International Journal of Multiphase Flow;(United Kingdom)*, *8*(1). https://doi.org/10.1016/0301-9322(82)90009-X

Brackbill, J. U., Kothe, D. B., & Zemach, C. (1992). A continuum method for modeling surface tension. *Journal of Computational Physics*, *100*(2), 335-354. https://doi.org/10.1016/0021-9991(92)90240-Y

Cavallini, A., Censi, G., Del Col, D., Doretti, L., Longo, G. A., & Rossetto, L. (2002). Condensation of halogenated refrigerants inside smooth tubes. *Hvac&R Research*, *8*(4), 429-451. https://doi.org/10.1080/10789669.2002.10391299

Chalfi, T. Y., & Ghiaasiaan, S. (2008). Pressure drop caused by flow area changes in capillaries under low flow conditions. *International Journal of Multiphase Flow*, *34*(1), 2-12. https://doi.org/10.1016/j.ijmultiphaseflow.2007.09.004

Chen, Y., Chu, M.-C., Liaw, J. S., & Wang, C. C. (2008a). Two-phase flow characteristics across sudden contraction in small rectangular channels. *Experimental thermal and fluid science*, *32*(8), 1609-1619. https://doi.org/10.1016/j.expthermflusci.2008.05.009

Chen, Y., Yang, K. S., Chang, Y.-J., & Wang, C. C. (2001). Two-phase pressure drop of air–water and R-410A in small horizontal tubes. *International Journal of Multiphase Flow*, *27*(7), 1293-1299. https://doi.org/10.1016/S0301-9322(01)00004-0

Cheng, L., Ribatski, G., Quibén, J. M., & Thome, J. R. (2008b). New prediction methods for CO2 evaporation inside tubes: Part I–A two-phase flow pattern map and a flow pattern based phenomenological model for two-phase flow frictional pressure drops. *International Journal of Heat and Mass Transfer*, *51*(1-2), 111-124. https://doi.org/10.1016/j.ijheatmasstransfer.2007.04.002

Chisholm, D. (1967). A theoretical basis for the Lockhart-Martinelli correlation for two-phase flow. *International Journal of Heat and Mass Transfer*, *10*(12), 1767-1778. https://doi.org/10.1016/0017-9310(67)90047-6

Chisholm, D. (1985). Two-phase flow in heat exchangers and pipelines. *Heat transfer engineering*, *6*(2), 48-57. https://doi.org/10.1080/01457638508939624

El-Shaboury, A., Soliman, H., & Sims, G. (2007). Two-phase flow in a horizontal equal-sided impacting tee junction. *International Journal of Multiphase Flow*, *33*(4), 411-431. https://doi.org/10.1016/j.ijmultiphaseflow.2006.10.002

Friedel, L. (1979). *Improved friction pressure drop correlations for horizontal and vertical two-phase pipe flow.* European Two-Phase Group Meeting, Ispra, Italy.

Geiger, G. E. (1964). *Sudden contraction losses in single and two-phase flow* [Doctoral dissertation, University of Pittsburgh].

Hirt, C. W., & Nichols, B. D. (1981). Volume of fluid (VOF) method for the dynamics of free boundaries. *Journal of Computational Physics*, *39*(1), 201-225. https://doi.org/10.1016/0021-9991(81)90145-5

Hwang, C. Y. J., & Pal, R. (1997). Flow of two-phase oil/water mixtures through sudden expansions and contractions. *Chemical Engineering Journal*, *68*(2-3), 157-163. https://doi.org/10.1016/S1385-8947(97)00094-6

Kourakos, V., Rambaud, P., Chabane, S., Pierrat, D., & Buchlin, J. (2009). Two-phase flow modelling within expansion and contraction singularities. *Computational Methods in Multiphase Flow V*, *63*, 27. https://doi.org/10.2495/MPF090031

Lin, S., Kwok, C., Li, R. Y., Chen, Z. H., & Chen, Z. Y. (1991). Local frictional pressure drop during vaporization of R-12 through capillary tubes. *International Journal of Multiphase Flow*, *17*(1), 95-102. https://doi.org/10.1016/0301-9322(91)90072-B

Liu, C., Gao, Y. S., Dong, X. R., Wang, Y. Q., Liu, J. M., Zhang, Y. N., Cai, X. S., & Gui, N. (2019), Third generation of vortex identification methods: Omega and Liutex/Rortex based systems. *Journal of Hydrodynamics*, *31*, 205-223. https://doi.org/10.1007/s42241-019-0022-4

Liu, C., Wang, Y., Yang, Y., & Duan, Z. (2016). New omega vortex identification method. *Science China Physics, Mechanics & Astronomy*, *59*, 1-9. https://doi.org/10.1007/s11433-016-0022-6

Mandhane, J., Gregory, G., & Aziz, K. (1974). A flow pattern map for gas—liquid flow in horizontal pipes. *International Journal of Multiphase Flow*, *1*(4), 537-553. https://doi.org/10.1016/0301-9322(74)90006-8

McAdams, W., Woods, W., & Heroman Jr, L. (1942). Vaporization inside horizontal tubes—II benzene-oil mixtures. *Transactions of the American Society of Mechanical Engineers*, *64*(3), 193-199. https://doi.org/10.1115/1.4019013

Mishima, K., & Hibiki, T. (1996). Some characteristics of air-water two-phase flow in small diameter vertical tubes. *International Journal of Multiphase Flow*, *22*(4), 703-712. https://doi.org/10.1016/0301-9322(96)00010-9

Monni, G., De Salve, M., & Panella, B. (2014). Horizontal two-phase flow pattern recognition. *Experimental Thermal and Fluid Science*, *59*, 213-221. https://doi.org/10.1016/j.expthermflusci.2014.04.010

Moreno Quiben, J. (2005). *Experimental and analytical study of two-phase pressure drops during evaporation in horizontal tubes.* EPFL.

Ong, C. L., & Thome, J. (2011). Macro-to-microchannel transition in two-phase flow: Part 1–Two-phase flow patterns and film thickness measurements. *Experimental Thermal and Fluid Science*, *35*(1), 37-47. https://doi.org/10.1016/j.expthermflusci.2010.08.004

Padilla, M., Revellin, R., & Bonjour, J. (2013). Two-phase flow of HFO-1234yf, R-134a and R-410A in sudden

contractions: Visualization, pressure drop measurements and new prediction method. *Experimental Thermal and Fluid Science*, *47*, 186-205. https://doi.org/10.1016/j.expthermflusci.2013.01.015

Patra, S. K., Roul, M. K., Satapathy, P. K., & Barik, A. K. (2021). Fluid dynamics and pressure drop prediction of two-phase flow through sudden contractions. *Journal of Fluids Engineering*, *143*(9), 091401. https://doi.org/10.1115/1.4050962

Quibén, J. M., & Thome, J. R. (2007a). Flow pattern based two-phase frictional pressure drop model for horizontal tubes, Part II: New phenomenological model. *International Journal of Heat and Fluid Flow*, *28*(5), 1060-1072. https://doi.org/10.1016/j.ijheatfluidflow.2007.01.004

Quibén, J. M., & Thome, J. R. (2007b). Flow pattern based two-phase frictional pressure drop model for horizontal tubes. Part I: Diabatic and adiabatic experimental study. *International Journal of Heat and Fluid Flow*, *28*(5), 1049-1059. https://doi.org/10.1016/j.ijheatfluidflow.2007.01.003

Roul, M. K., & Dash, S. K. (2011). Two-phase pressure drop caused by sudden flow area contraction/expansion in small circular pipes. *International Journal for Numerical Methods in Fluids*, *66*(11), 1420-1446. https://doi.org/10.1002/fld.2322

Schmidt, J., & Friedel, L. (1997). Two-phase pressure drop across sudden contractions in duct areas. *International Journal of Multiphase Flow*, *23*(2), 283-299. https://doi.org/10.1016/S0301-9322(96)00056-0

Shannak, B. A. (2008). Frictional pressure drop of gas liquid two-phase flow in pipes. *Nuclear Engineering and Design*, *238*(12), 3277-3284. https://doi.org/10.1016/j.nucengdes.2008.08.015

Song, X., Ma, J., Li, Y., Sun, X., & Zhao, Y. (2023). Analysis of the flow phenomenon of fluid undergoing a sudden contraction to an annular gap. *Physics of Fluids*, *35*(9). https://doi.org/10.1063/5.0169034

Taitel, Y., & Dukler, A. E. (1976). A model for predicting flow regime transitions in horizontal and near horizontal gas-liquid flow. *AIChE Journal*, *22*(1), 47-55. https://doi.org/10.1002/aic.690220105

Vallée, C., Höhne, T., Prasser, H.-M., & Sühnel, T. (2008). Experimental investigation and CFD simulation of horizontal stratified two-phase flow phenomena. *Nuclear Engineering and Design*, *238*(3), 637-646. https://doi.org/10.1016/j.nucengdes.2007.02.051

Zahedi, R., & Rad, A. B. (2022) Numerical and experimental simulation of gas-liquid two-phase flow in 90-degree elbow. *Alexandria Engineering Journal*, *61*(3):, 2536-2550. https://doi.org/10.1016/j.aej.2021.07.011

Zeghloul, A., Azzi, A., Hasan, A., & Azzopardi, B. J. (2018). Behavior and pressure drop of an upwardly two-phase flow through multi-hole orifices. *Proceedings of the Institution of Mechanical Engineers, Part C: Journal of Mechanical Engineering Science*, *232*(18), 3281-3299. https://doi.org/10.1177/0954406217736081

Zeghloul, A., Azzi, A., Saidj, F., Messilem, A., & Azzopardi, B. J. (2017). Pressure drop through orifices for single-and two-phase vertically upward flow—implication for metering. *Journal of Fluids Engineering*, *139*(3), 031302. https://doi.org/10.1115/1.4034758

Zeghloul, A., Bouyahiaoui, H., Azzi, A., Hasan, A. H., & Al-sarkhi, A. (2020). Experimental investigation of the vertical upward single-and two-phase flow pressure drops through gate and ball valves. *Journal of Fluids Engineering*, *142*(2), 021401. https://doi.org/10.1115/1.4044833

Zhang, Y. N., Wang, X. Y., Zhang, Y. N., & Liu, C. (2019). Comparisons and analyses of vortex identification between Omega method and Q criterion. *Journal of Hydrodynamics*, *31*, 224-230. https://doi.org/10.1007/s42241-019-0025-1

Zhang, Y., He, C., & Li, P. (2021). Numerical investigation of gas-liquid two-phase flow in horizontal pipe with orifice plate. *Progress in Nuclear Energy*, *138*, 103801. https://doi.org/10.1016/j.pnucene.2021.103801

APPENDIX

The expression of the Abdelall correlation (Abdelall et al., 2005) is shown in Eq. (31):

$$\Delta p_c = G_2^2 \left[\frac{\rho_{tp}\left(\frac{1}{C_c^2} - \sigma_A^2\right)}{2\rho''^2} + \frac{1-C_c}{\rho'} \right] \tag{31}$$

where:

$$\rho_{tp} = \left(\frac{x}{\rho_G} + \frac{1-x}{\rho_L} \right)^{-1} \tag{32}$$

$$\rho' = \left[\frac{1-x^2}{\rho_L(1-\varepsilon)} + \frac{x^2}{\rho_G \varepsilon} \right]^{-1} \tag{33}$$

$$\rho'' = \left[\frac{(1-x)^3}{\rho_L^2(1-\varepsilon)^2} + \frac{x^3}{\rho_G^2 \varepsilon^2} \right]^{-1/2} \tag{34}$$

$$S = \frac{x}{1-x}\frac{1-\varepsilon}{\varepsilon}\frac{\rho_L}{\rho_G} = \left(\frac{\rho_L}{\rho_G}\right)^{1/3} \tag{35}$$

The Padilla correlation (Padilla et al., 2013) is shown as Eq. (36):

$$\Delta p_c = \Delta p_{sing} + \Delta p_{mom} + \Delta p_{pert} \tag{36}$$

where:

$$\Delta p_{\text{mom}} = \frac{x^2}{\rho_{\text{G}}}\left(\frac{G_2^2}{\varepsilon_2} - \frac{G_1^2}{\varepsilon_1}\right) + \frac{(1-x)^2}{\rho_{\text{L}}}\left[\frac{G_2^2}{(1-\varepsilon_2)} - \frac{G_1^2}{(1-\varepsilon_1)}\right] \tag{37}$$

$$\varepsilon = \frac{x}{\rho_{\text{G}}}\left\{[1+0.12(1-x)]\left(\frac{x}{\rho_{\text{G}}} + \frac{1-x}{\rho_{\text{L}}}\right) + \frac{1.18(1-x)\left[g\gamma(\rho_{\text{L}}-\rho_{\text{G}})\right]^{0.25}}{G\rho_{\text{L}}^{0.5}}\right\}^{-1} \tag{38}$$

$$\Delta p_{\text{sing}} + \Delta p_{\text{pert}} = K_{\text{L}}\Delta p_{\text{L}} + K_{\text{G}}\Delta p_{\text{G}} \tag{39}$$

$$K_{\text{L}} = \left[b(1-x)(1-x^a)\right](1-\sigma_{\text{A}})^c \tag{40}$$

$$K_{\text{G}} = \left[ax^b + bx^a(1-x)\right](1-\sigma_{\text{A}})^c \tag{41}$$

$$\Delta p_{\text{L}} = \frac{G_2^2(1-x)^2}{\rho_{\text{L}}(1-\varepsilon_2)^2} \tag{42}$$

$$\Delta p_{\text{G}} = \frac{G_2^2 x^2}{\rho_{\text{G}}\varepsilon_2^2} \tag{43}$$

In Eqs. (40) and (41), take a = 0.0017; b = 2; and c = 1/4.

The Schmidt and Friedel correlations (Schmidt & Friedel, 1997) are expressed as Eq. (44):

$$\Delta p_{\text{c}} = \frac{G_2^2\left\{\frac{1-\sigma_{\text{A}}}{\rho_{\text{eff}}} + f_{\text{c}}\rho_{\text{eff}}\left[\frac{x}{\rho_{\text{G}}\varepsilon} - \frac{1-x}{\rho_{\text{L}}(1-\varepsilon)}\right]^2\left(1-\sigma_{\text{A}}^{1/2}\right)^2\right\}}{1+\Gamma_{\text{c}}\left(\frac{1}{\sigma_{\text{A}}}-1\right)} \tag{44}$$

where:

$$\frac{1}{\rho_{\text{eff}}} = \frac{x^2}{\rho_{\text{G}}\varepsilon} + \frac{(1-x)^2}{\rho_{\text{L}}(1-\varepsilon)} + \rho_{\text{L}}(1-\varepsilon)\left(\frac{\alpha_{\text{E}}}{1-\alpha_{\text{E}}}\right)\left[\frac{x}{\rho_{\text{G}}\varepsilon} - \frac{1-x}{\rho_{\text{L}}(1-\varepsilon)}\right]^2 \tag{45}$$

$$\varepsilon = 1 - \frac{2(1-x)^2}{1-2x+\sqrt{1+4x(1-x)\left(\frac{\rho_{\text{L}}}{\rho_{\text{G}}}-1\right)}} \tag{46}$$

$$\alpha_{\text{E}} = \frac{1}{S}\left[1 - \frac{1-x}{1-x(1-0.18\text{We}^{0.27}\text{Re}^{0.5})}\right] \tag{47}$$

$$S = \frac{x}{1-x}\frac{1-\varepsilon}{\varepsilon}\frac{\rho_{\text{L}}}{\rho_{\text{G}}} \tag{48}$$

$$\text{We} = G_2^2 x^2 \frac{D_2}{\rho_{\text{G}}\gamma}\frac{(\rho_{\text{L}}-\rho_{\text{G}})}{\rho_{\text{G}}} \tag{49}$$

$$\text{Re} = \frac{G_2(1-x)D_2}{\mu_{\text{L}}} \tag{50}$$

$$\Gamma_{\text{c}} = 0.77\sigma_{\text{A}}(1-\sigma_{\text{A}}^{0.306}) \tag{51}$$

$$f_{\text{c}} = 0.0052x^{0.1}(1-x)\left(\sigma_{\text{A}}\frac{\mu_{\text{L}}}{\mu_{\text{G}}}\right)^{0.8} \tag{52}$$